Journal of Materials Chemistry C

PAPER

View Article Online
View Journal | View Issue

Cite this: J. Mater. Chem. C, 2018, 6, 1959

Controlling the crystallinity and crystalline orientation of "shuttlecock" naphthalocyanine films for near-infrared optoelectronic applications†

Simon Dalgleish, ‡*[ab] Louisa Reissig,[ac] Yoshiaki Shuku,[a] Christophe Gourlaouen,[d] Sergi Vela[d] and Kunio Awaga*[a]

Received 1st December 2017,
Accepted 22nd January 2018

DOI: 10.1039/c7tc05521h

rsc.li/materials-c

The thin film properties of tin(II) 2,3-naphthalocyanine (SnNPc) were interrogated and various strategies for controlling the crystallinity and crystalline orientation within the films were assessed. SnNPc is shown to crystallize in the space group $P2_1/c$ (Z = 4), where the molecular arrangement consists of alternating layers of concave and convex overlap, induced by the out-of-plane Sn atoms, resulting in a 3D slipped-π-stack network structure analogous to that reported for Phase I of titanyl phthalocyanine. The thin films were studied by X-ray diffraction, atomic force microscopy and absorption spectroscopy and are highly sensitive not just to the conditions during growth, but also to substrate pre- and post-deposition treatment. While the films grown at room temperature were largely amorphous, the crystallinity was enhanced with substrate temperature, with the molecules orienting in a standing molecular geometry. A thin layer of 3,4:9,10-perlenetetracarboxylic dianhydride induces a lying molecular geometry of the same polymorph as that of the single crystal, while different polymorphs are accessible through solvent vapor annealing of amorphous films. Transient photocurrent measurements showed a dramatic improvement in photodetector device bandwidth for the lying molecular geometry, which was attributed to enhanced photoconductivity along the π-stacking axis, while solvent vapor annealing could be used to tune the photosensitivity across the near-infrared region.

Introduction

The ability to control the orientation of functional molecules in thin films, both with respect to neighboring molecules and to the substrate surface, is essential for the optimization of material performance in their intended application and device configuration. For organic semiconductors, a highly planar molecular structure is common, resulting from extensive sp^2 hybridization, and the angle and proximity with which the molecules approach each other in the solid-state (and their frontier orbitals interact) is critical for efficient charge transfer between molecules.[1–4] Furthermore, the anisotropic properties of many organic crystals suggests that device performance would be significantly enhanced if the stacking axis were aligned with the direction of charge movement, and/or the transition dipoles of the chromophores aligned for maximum optical absorption.[5–9]

The phthalocyanines (Pcs), as a representative class of functional molecules, show rich polymorphism with significant consequences on their colligative properties. The planar free-base Pc (H_2Pc), and those of the divalent 1st row transition metals (MPc; M = Mn, Fe, Co, Ni, Cu, Zn) are known to crystallize in at least two dominant polymorphic forms: α and β (both herringbone packed along the *b*-axis, which lies parallel to the substrate, but which differ in the tilt angle between the *b*-axis and the molecular plane).[10] While the α polymorph is generally achieved by physical vapor deposition on substrates held at room temperature, the β polymorph is favored at higher temperatures, and/or by post-deposition annealing.[11,12] In the case of the non-planar Pcs of large and tetravalent metals

[a] Department of Chemistry and IRCCS, Nagoya University, Furo-cho, Chikusa, 464-8602 Nagoya, Japan. E-mail: simondalgleish@gmail.com, awaga@mbox.chem.nagoya-u.ac.jp
[b] Institute for Advanced Research, Nagoya University, Furo-cho, Chikusa, 464-8601 Nagoya, Japan
[c] Institute of Experimental Physics, Freie Universität Berlin, Arnimallee 14, 14195 Berlin, Germany
[d] Laboratoire de Chimie Quantique, Institut de Chimie, UMR 7177 CNRS-Université de Strasbourg, 4 rue Blaise Pascal, 67081 Strasbourg, France

† Electronic supplementary information (ESI) available: Further experimental details as well as additional experimental data on the molecular structure and packing, thin film characterization, computational analysis and device performance CCDC 1587466 and 1587467. For ESI and crystallographic data in CIF or another electronic format see DOI: 10.1039/c7tc05521h

‡ SD has since moved to Humboldt-Universität zu Berlin, Germany.

(*e.g.* M = Sn, Pb, VO, TiO), at least three polymorphic forms have been identified (Phase I[13] and Phase II[13] fully resolved, and Phase Y[14] proposed by Rietveld refinement). The different polymorphs are accessible through tuning of the deposition conditions,[15,16] or by the transformation of amorphous films by *i.a.* solvent vapor annealing.[17–19] While Phase I shows an absorption profile broadly similar to that of the amorphous films, Phase II and Y show an extreme red-shift to their Q-band absorption, extending beyond 800 nm, making such films of technological interest for optical data transmission and storage. These latter phases have also been shown to yield significant improvements in J_{sc} for organic photovoltaic cells, due to a broader spectral coverage.[20–23]

An alternative strategy to red-shifted absorption is *via* π-extension through benzanulation, and the naphthalocyanines (NPcs) have been shown to absorb efficiently between 700 and 900 nm, even as amorphous films.[24] Compared to the Pcs, the NPcs have been relatively less studied, due, in part, to their higher sublimation temperatures that are close to the limits of their thermal stability.[24] As a result, few NPc crystal structures have been reported. Morishige *et al.* succeeded in resolving crystals of Ni, Cu, and ZnNPc,[25] which are isostructural and monoclinic ($P2_1/c$; $Z = 2$), forming a 2-dimensional stacking sheet within the *ab* plane, in contrast to the 1-dimensional stacking for the analogous Pcs. Several previous studies have investigated the orientation of NPcs on various substrates by high-resolution electron microscopy, and have shown that both the nature and temperature of the substrate during deposition can influence the crystalline structure of such films.[26,27] Yanagi *et al.* have shown that ZnNPc can orient with the molecular planes perpendicular, parallel and inclined to the substrate normal when deposited on glass, NaCl and highly oriented pyrolytic graphite, respectively.[26] Furthermore, they have also shown that VONPc undergoes a transition from amorphous to standing to epitaxial, when deposited on KCl, at substrate temperatures ranging from room temperature up to 300 °C.[27] However, for device application it would be advantageous to develop a platform for structural control that is independent of the substrate material.

Recently, molecular templating has been demonstrated as an efficient method for controlling the crystallinity and crystalline orientation of organic thin films, whereby a thin conditioning layer is applied to a substrate, prior to film deposition, that influences the growth of the functional film through π-stacking and/or electrostatic interactions. Various materials have been investigated to serve this purpose, including multiphenyl- and multithiophene-based templates, perylene derivatives, acenes, and 2-D materials such as graphene.[28,29] Within these studies, 3,4:9,10-perlenetetracarboxylic dianhydride (PTCDA) has emerged as an efficient template for inducing a parallel stacking for a range of π-conjugated organic molecules.[30,31] PTCDA is known to deposit (predominantly) in the α-polymorph as cofacial stacks, inclined from the substrate surface by 11°, making the 102 plane parallel to the substrate normal.[32] This arrangement has been shown to induce molecular stacking of Pc molecules perpendicular to the substrate,[33,34] in contrast to the parallel stacking common to Pcs deposited on untemplated substrates. As such, the resultant Pc films are ideally arranged for stacked optoelectronic devices such as photovoltaics and photodetectors, and various groups have reported significant gains in device performance due to improved light harvesting and charge management within the Pc devices.[35–37]

In this study, we expand the scope of molecular templating with PTCDA to the naphthalocyanines (NPcs). Specifically, we focus on Sn(II)NPc (SnNPc), which shows a further red-shift in its absorption profile beyond that imparted by benzanulation due to the out-of-plane metal center, and resultant deformation to the molecular skeleton. Such ''shuttlecock'' NPcs (which include GeNPc and PbNPc, VONPc) show a common absorption profile in the solid state centered around 850 nm (770 nm shoulder), which is ideally placed for short distance fiber-optic communication. The factors governing the crystallinity and crystalline orientation of the thin films of SnNPc are explored, and their effect on device performance is assessed in photodetectors of a structure metal/insulator/semiconductor/metal (MISM).[38] The results are additionally compared to previous work and unpublished data (see ESI†) on the thin film properties of VONPc that have previously been studied for MISM photodetection.[39]

Materials and methods

General methods

SnNPc and VONPc were purchased from Sigma Aldrich, and used as received. All substrates were cleaned by mild bath ultrasonication ($P = 45$ W, 0.5% Helmanix III solution, acetone, methanol, 10 min each) and blown dry with nitrogen. Unless otherwise stated, all substrates were further subjected to UV/ozone cleaning (Bioforce Nanosciences ProCleanerPLUS, 10 min) immediately prior to deposition.

Single crystals of SnNPc were grown from the commercial sample by flow sublimation. Specifically, 40 mg of material was loaded into a quartz boat and inserted into a two-stage tube furnace under a flow of N_2. The boat was positioned in the first furnace, which was ramped to 480 °C, while the second furnace was held at 250 °C.

Organic films were fabricated under physical vapor deposition (PVD) at a base pressure of $< 4 \times 10^{-4}$ Pa by resistive heating of a ceramic crucible to induce sublimation. The substrates were fixed at a height of 20 cm above the crucible on a heated substrate holder. In this arrangement, the substrates reached a maximum temperature of 45 °C during the deposition cycle. When the substrate holder was set at 50 °C, this effect of radiative heating was negligible, and thus the substrate temperature could be varied between 50–200 °C with a precision of ±2 °C. The growth rate was monitored using a quartz crystal microbalance (QCM), calibrated as described below. For the bilayer films used for characterization, the vacuum could be broken between layer depositions, and the films stored in a vacuum desiccator for up to a week showed no observable change in their characterization data.

Molecular & bulk characterization

Single crystal X-ray diffraction (XRD) was performed on a Rigaku RA-Micro007 with a Saturn CCD detector using

graphite-monochromated Mo Kα radiation (λ = 0.71075 Å). The crystals were mounted on a glass fiber using an epoxy adhesive (Araldite Rapid, Huntsman Japan, Kobe, Japan), and set under a nitrogen stream. A full refinement was performed at −153 °C and 27 °C, and the unit cell parameters were recorded at 20 °C intervals over this range. The frame data were integrated and corrected for absorption with the Rigaku/MSC CrystalClear package.[40] The structures were solved by direct methods[41] and standard difference map techniques, and were refined with full-matrix least-square procedures on F^2 by using the Rigaku/MSC CrystalStructure package.[40] Anisotropic refinement was applied to all non-hydrogen atoms. All hydrogen atoms were placed at the calculated positions and refined using a riding model. Full details of the structure refinement are given in Table S1 (see ESI†). CCDC 1587466 and 1587467.†

Solution absorption spectra were measured on a Shimadzu UV-3100PC spectrophotometer for SnNPc and VONPc dissolved in 1-chloronaphthalene using a quartz cell (L = 1 cm).

Film characterization

Film thicknesses were estimated for each deposition condition (for QCM validation) by surface profilometry using a stylus-type step profiler (Dektak 150, scan speed = 4 μm s^{-1}, stylus force = 1 mg) on clean glass substrates (thick films $>$20 nm), and X-ray reflectivity (thin films $<$50 nm). Reflectivity measurements were performed using Cu Kα radiation (λ_{av} = 1.541874 Å, 40 kV, 30 mA) on a Rigaku Smartlab X-ray diffractometer employing parallel-beam optics (scan range 0–10°, step 0.01° at 0.3° min^{-1}). Data were analyzed using the GlobalFit firmware.[42]

Thin film XRD (Rigaku Smartlab, same optics as for reflectivity) was recorded for films on 10 × 10 mm silicon wafers with a 400 nm thermally grown layer of SiO_2 (herein referred to as SiO_2). Measurements were performed in symmetrical reflection mode ($2\theta/\theta$), scanning the range 2–35° (step 0.02° at 0.2° min^{-1}), unless otherwise stated (see ESI†). Data were analyzed using the PDXL firmware.[42]

Atomic force microscopy (AFM) was measured using a Bruker Dimension FastScan AFM system with Fastscan-C Probes. Samples were usually scanned twice in tapping mode at 2 sampling points (scan area 0.5 × 0.5 μm, and 1 × 1 μm, 384 or 512 lines, scan speed $\leq$0.5 Hz, optimized for high resolution of the specific surface). For optically inhomogeneous samples (such as partially crystallized samples or those showing phase separation) a scan area of $\geq$10 × 10 μm was chosen before zooming into the distinct regions. Images were analyzed using the Nanoscope Analysis software.[43] When necessary the images were level corrected. The surface roughness parameters (R_a, R_z and R_{max}) were determined from at least 3 cross-sections.

Thin-film absorption measurements (Shimadzu UV-3100PC) were recorded on 10 × 10 mm quartz substrates in transmission mode, with the beam profile reduced using a perforated plate (∅ = 6.5 mm), and with substrates fixed normal to the incident beam.

It should be noted that once the processing conditions were optimized, the characterization data reported were consistent over at least two separate batches.

Computational details

The crystal structure resolved at −153 °C was fully optimized (*i.e.* atomic nuclei and cell parameters) using the Quantum Espresso package (QE) Version 5.2, employing the PBE+D2 scheme, Vanderbilt pseudopotentials, a Γ-point sampling of the Brillouin zone and a kinetic energy cutoff of 70 Ry. Beyond the monomer, several clusters including two (dimer) and four (tetramer) SnNPc molecules were extracted from the resulting optimized cell. The monomer was further optimized in solvent (1-chloronaphthalene) conditions, which was described using the PCM model with a dielectric constant of 5.04 Debye and a radius of 3.78 Å (and N_{eql} = 2.66 for the TD-DFT). The absorption spectra were computed by means of TD-DFT, using the B3LYP functional[44] with scalar relativistic effects (ZORA Hamiltonian)[45] and a TZP all electron Slater basis set,[46] as implemented in ADF 2013.[47] Eighty roots were computed with the aim of describing the near-infrared (NIR) region of the absorption spectra at a moderate computational cost, and the simulated spectra were convoluted using Gaussian functions (σ = 10 nm). To characterize the nature of the transition, the electronic density difference between the ground state and the excited states was computed by subtracting the electron density of the ground state from that of the excited states. The electronic densities of states and differences were computed using the DGRID package.[48]

Device fabrication & testing

The various films for device testing were grown in an identical manner to that described above on patterned indium tin oxide (ITO) glass substrates (15 × 15 mm (substrate) with two 2 mm strips of ITO), pre-cleaned as described above. For bilayer films, the vacuum was not broken between layers, and comparisons between the single layer and bilayer devices were made through the use of a shutter system during deposition. The devices were assembled in a stacked architecture, where a silver counter electrode (2 mm strip deposited at 0.5 Å s^{-1} to a thickness of 200 nm on a 10 × 20 mm glass substrate) was fixed on top and perpendicular to the ITO/film electrode with a thermally sealable 60 μm Surlyn spacer (Solaronix), as shown in Fig. S1 (ESI†). The device was completed immediately prior to measurement by filling the void between the electrodes with the ionic liquid *N*-(2-methoxyethyl)-*N*-methylpyrrolidinium bis(trifluoromethanesulfonyl)imide (MEMP-TFSI), received as a gift from Nisshinbo Holdings Inc.

Photocurrent measurements were performed to scrutinize: (1) the photocurrent waveforms resulting from SnNPc excitation, and (2) the wavelength-dependent photocurrent response (action spectra) using the homebuilt setups previously reported,[39,49] and further described in the ESI.† In short:

(1) The devices were illuminated with an LED light source (λ_{max} = 850 nm) modulated as a square-wave signal. The generated photocurrent response was amplified using a transimpedance amplifier (Femto DHPCA100), and visualized on an oscilloscope (Tektronix TDS5104B) in high resolution mode. The measurements were made over a frequency range of 1 Hz–100 kHz, and the stability (within 10%) within the

experimental timespan confirmed. In all measurements the Ag counter electrode was grounded, *i.e.* a positive signal corresponds to the movement of holes from the semiconductor electrode, *via* the external circuit, to the counter electrode, with accumulation of electrons at the semiconductor/insulator interface.

(2) Action spectra measurements were performed immediately following the LED experiments. The devices were illuminated by a tungsten/halogen light source (Spectral Products ASBN-W 100 L) attached to a monochromator (Digikröm CM110, slits 1.2 and 0.6 mm, resolution 8–10 nm), and modulated by a chopper (NF Corp. 5584A) at 90.5 Hz. The photocurrent signals were extracted using a lock-in amplifier (NF 5610B/A), pre-amplified using a low noise transimpedance amplifier (Femto, DLPCA 200) and recorded on a computer. The setup was controlled by a home-written LabVIEW program, scanning the wavelength range from 1400 to 400 nm (step 2 nm at 2s per step) in both directions. The data were analyzed by averaging between the forth and back scan (which showed in general high similarity, confirming the stability of the devices), and dividing by the wavelength-dependent light power to obtain the responsivity spectra.

Results & discussion

Molecular structure and packing

Black block-shaped crystals of SnNPc were grown under train sublimation at 480 °C. A single polymorph was identified from multiple crystals, and indexed as $P2_1/c$ ($Z = 4$). The molecular structure of SnNPc at −153 °C is shown in Fig. 1a (*cf.* Table S1, ESI†). The coordination geometry around the Sn atom is

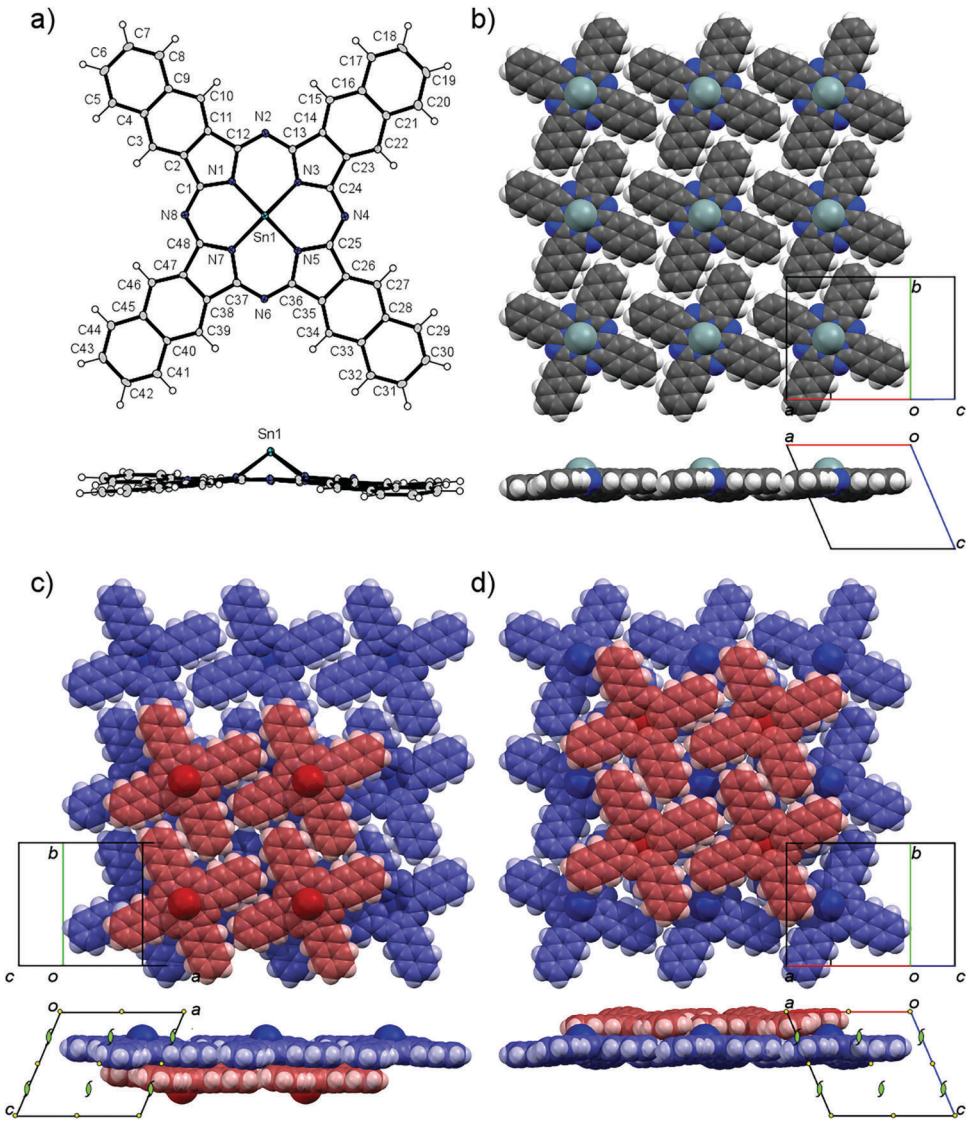

Fig. 1 (a) Molecular structure of SnNPc measured at −153 °C: (b) molecular packing of SnNPc along the *ab* plane, which is perpendicular to π–π overlaps; (c and d) two different motifs of π-overlaps: concave (c) and convex (d). Inversion centers (yellow symbols) and two-fold screw axes (green symbols) are shown in the view from the *b* axis.

deviated square planar, with Sn–N bond distances of 2.245(2)–2.257(3) Å (Table S2, ESI†), and the distance between the Sn atom and the least-squares (LS) plane of coordinated nitrogen atoms of 1.09 Å. These values are similar to those of SnPc (2.260(7)–2.273(5) Å and 1.11 Å, respectively).[50,51] The averaged bond lengths of SnNPc shown in Fig S2 (ESI†) exhibit a characteristic bond alternation in the naphthalene rings, which is consistent with those observed for the other resolved MNPcs.[25] However, for SnNPc, the angles between the naphthalene LS planes and the LS plane of coordinated nitrogen atoms are slightly distorted by 2.53–7.76°, as shown in Table S2 (ESI†).

Fig. 1b shows the packing structure of the SnNPc molecules, where the molecules are arranged in layered sheets. All SnNPc molecules in a layer can be related by parallel translation, and thus they orientate to the same direction. This two sided plane without mirror symmetry can be regarded to have plane chirality. Fig. 1c and d show the two different inter-layer arrangements for concave and convex overlap, where the layers align parallel (d = 3.04 Å) and alternatingly inclined ($\angle$ = 7.59°), respectively. The side views of the layer structure show the inversion centers and 2-fold screw axes locating between the layers (Fig. 1c and d bottom). The racemic overlap arrangements related by inversion centers (Fig. 1c) and the chiral overlap arrangements related by 2-fold screw axes (Fig. 1d) appear alternately in the stacking direction. The molecular structure and packing is analogous to that of Phase I of TiOPc, resolved by Hiller *et al.*[13] In this case, the attractive interaction of the π-systems, which dominates the structure of the planar Pcs resulting in 1D stacking, is opposed by the steric effect of the out-of-plane TiO (or Sn) center, rendering slipped dimers in the case of the concave pairs, and a 4-fold peripheral overlap in the case of the convex pairs. Such a steric disruption to π-stacking has been explored extensively by Inabe *et al.* to increase the dimensionality of Pc-based conductors through the use of axial ligation to planar Pcs.[52]

The single crystal data are consistent with the powder diffraction pattern measured for the commercial sample used in this study in terms of peak progression and relative peak intensity (Fig. S3, ESI†), with all peaks clearly resolved, and no peaks originating from other polymorphs. However, the lattice parameters of the single crystal appear contracted, especially in the c axis. By measuring the single crystal at increasing temperature between −153 °C and 27 °C, the peaks tended towards the powder data, with a predominant expansion in the c axis (Fig. S4, ESI†). An analogous thermal expansion has also been observed for Phase I TiOPc,[18,19] and suggests a relative flexibility in the NPc molecules within the crystal.

Despite numerous attempts, no crystals of VONPc suitable for XRD analysis could be achieved. However, by comparing the powder spectrum of VONPc to that obtained for SnNPc, as shown in Fig. S5 (ESI†), distinct similarities can be observed between the two spectra, especially in the long angle region. The spectra show identical peaks at 27.0° (014), 26.4° (004) and 20.5° (013). The peak at 26.4° is especially characteristic since it approximates the layering structure of SnNPc (3.34 Å). On the basis of this, it is possible to rule out a Phase II structure (the only polymorph identified for VOPc),[53] since a peak corresponding to the interplanar distance ($\bar{2}12$) at 28.7° is missing. Furthermore, the structure seems distinct from that proposed by Yanagi *et al.* for VONPc on KCl, based on high resolution electron diffraction,[27] since neither the stacking axis (010, d = 3.8 Å) nor the interplanar distance (d = 3.74 Å) would yield a peak at 26.4°. However, in order to correctly identify the structure of VONPc, we await a crystal suitable for a full structural refinement.

Thin film characterization

As deposited films. SnNPc deposited stably over a range of deposition rates, and no evidence of decomposition (or other impurities) was observed by transmission FTIR of the films deposited on KBr disks. The films deposited at room temperature at a deposition rate of 0.5 Å s^{-1} were largely amorphous. By maintaining a substrate temperature of 50 °C (the minimum temperature where radiant heating from the effusion cell had no effect), and employing a slow rate of 0.1 Å s^{-1}, a weak diffraction at $2\theta \approx 6°$ was observed on a range of common substrates (Au, Ag, Al, ITO, parylene-C), which was enhanced with substrate temperature during deposition. Fig. 2a shows the evolution of the XRD pattern with substrate temperature for 100 nm thick films of SnNPc deposited on SiO_2 substrates. At 200 °C, the peak at 6.0° is clearly resolved, and two additional weak diffractions appear, centered around ~12° and 26.4°.

Fig. 2b and c shows the AFM image of SnNPc deposited at 50 °C and 200 °C, respectively. At 200 °C, large discreet irregular crystallites of the order of 100 nm are clearly observed, yielding a surface roughness (R_z) of 45 nm. This structure is distinct from those grown at lower temperatures (Fig. S6, ESI†), which commonly show a featureless surface with a roughness of <5 nm. In Fig. 2d the absorption spectra of the SnNPc films grown at various substrate temperatures are shown, compared to the solution spectrum of SnNPc measured in 1-chloronaphthalene. The solution spectrum is characterized by an intense Q-band at λ_{max} = 829 nm, followed by a vibrational progression towards higher energy.[54] In the solid state, the Q-band is red-shifted to a λ_{max} = 860 nm, with a prominent shoulder at 780 nm. The spectra are relatively insensitive to the deposition rate, film thickness and substrate temperatures up to 150 °C, changing only in the red tail of the Q-band. For films deposited at 200 °C, the Q-band is further red-shifted and slightly diminished, with an additional peak emerging on the red tail of the Q-band.

All these data suggest minimal crystallinity for the as deposited film ≤150 °C. At a substrate temperature of 200 °C, the crystallinity of the film is increased, and the peaks observed in the XRD at 6.0° and ~12° would seem to correspond to the 100 and 200 planes, respectively, while the peak at 26.4° could indicate the orthogonal 004 plane, indexed from the single crystal data, suggesting a crystalline structure similar to Phase I TiOPc, adopting a (predominantly) standing geometry on the substrate, with crystallinity enhanced by the substrate temperature. By adopting different diffraction geometries, no other strong diffractions were observed in the asymmetric mode, and only weak diffractions could be resolved in in-plane mode, which are tentatively assigned to the $10\bar{2}$ and $20\bar{4}$ planes,

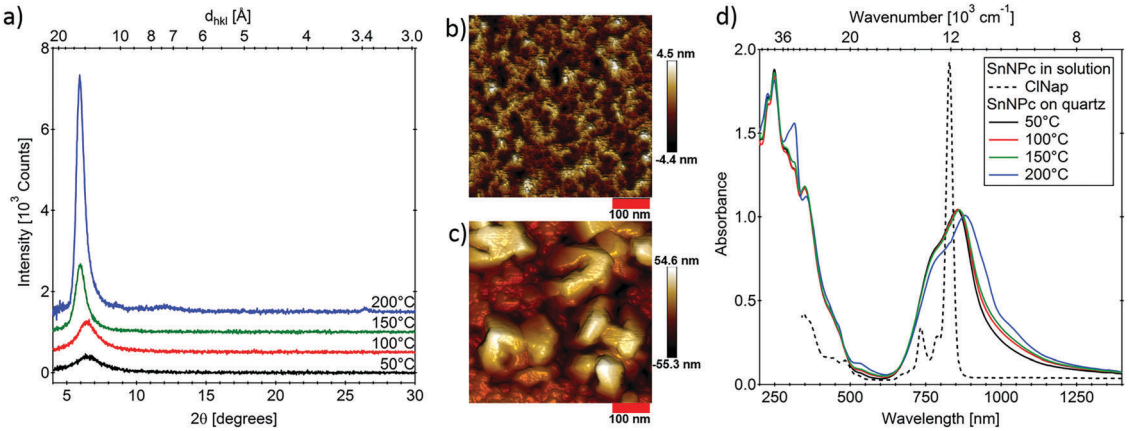

Fig. 2 Characterization of thin films of SnNPc (d = 100 nm, rate 0.1 Å s^{-1}) deposited at various substrate temperatures: (a) thin film XRD on SiO_2 substrates (data offset for clarity); (b and c) AFM images of films grown on SiO_2 at substrate temperatures of (b) 50 °C, and (c) 200 °C, red scale bars indicate 100 nm; (d) thin film absorption spectra on quartz substrates, compared to the solution spectrum (arbitrary scale), measured in 1-chloronaphthalene (ClNap).

nearly orthogonal to the 100, as well as a persistent peak from the 100 plane, confirming at least some degree of biaxial orientation (Fig. S7, ESI†). However, since the peak around 6° roughly corresponds to the orthogonal lattice dimensions of the a and c axis for VONPc (15.7 and 15.8 Å, respectively), reported by Yanagi *et al.*,[27] it is also possible that such films are composed of other manifestations of a standing molecular geometry. Interestingly, a similar crystallinity and orientation can be achieved post deposition from an amorphous film (grown at 0.5 Å s^{-1}) by solvent vapor annealing (SVA) with MeOH. Such films are analogous not only in their XRD pattern, but also in their absorption profile. Further details on SVA with MeOH and other solvents, which are shown to induce different crystalline phases, are given in the Supporting Information (*cf.* Fig. S8–S10, ESI†).

Compared to SnNPc, the crystallinity of VONPc films was significantly greater, with discreet crystallites already observable on substrates at room temperature (Fig. S11, ESI†). This crystallinity was enhanced with temperature, and a common peak in the thin film XRD is observed at $2\theta \approx 6^\circ$ (Fig. S12a, ESI†). However, unlike for SnNPc, a peak at 26.4° of similar intensity was observed over the entire temperature range studied. The positions of these peaks suggest a thin film structure distinct from that observed by Yanagi *et al.*,[27] who resolved a columnar stacking on KCl at elevated substrate temperatures. In this case, the latter peak would seem to correspond to the 004 plane in the crystal structure of SnNPc, as is prominent in both their powder diffractions (*cf.* Fig. S5, ESI†), suggesting the existence of both the standing and lying crystalline orientations. From the powder XRD data of VONPc, the intensity of the peak at 6° is several orders of magnitude weaker than that at 26.4°, thus the standing geometry still dominates the film. The relative heights of the 6° and 26.4° peaks are largely unaffected by the deposition temperature, but are sensitive to film thickness, with the 6° peak predominant in the early stages of growth. A likely reason for this is related to the deposition rate. The deposition of VONPc is self-limiting and, to achieve a thick film, an increased initial rate is required, which then diminishes as the deposition progresses (further increases in temperature do not significantly improve the rate, but eventually lead to a loss of film purity).[39] It seems, therefore, that in the case of VONPc, a fast rate favors a standing structure, whereas a lying structure is more favored at a slow rate, though it is still the minor crystalline orientation in the film.

The absorption spectra for relatively amorphous films of VONPc are structurally similar to those of SnNPc (excepting a larger absorption in the visible region), with λ_{max} = 845 nm, and a prominent shoulder at 780 nm. However, for VONPc the major Q-band appears sharper, and increases significantly with substrate temperature (Fig. S12b, ESI†). This is consistent with an increased crystalline component with molecular planes parallel to the substrate, and thus normal to the incident beam. A similar change in the absorption spectrum was also observed following SVA on relatively amorphous films (Fig. S13a, ESI†). Under all solvents tested, SVA resulted in an increase in crystallinity observed by AFM, and in all cases the resultant XRD patterns were consistent with that of the high temperature deposition (Fig. S13b, ESI†). It is likely that the small crystallites, observed down to room temperature, act as seed points during SVA that facilitate crystallization, but not a phase change.

At low substrate temperatures, both SnNPc and VONPc form relatively amorphous films, with almost identical spectroscopic properties which, in turn, are similar to those reported for other shuttlecock MNPcs.[24] In both cases, the film crystallinity is enhanced with substrate temperature, favoring a standing molecular geometry, with a likely crystalline structure of that resolved for single crystals of SnNPc, with the *bc* plane parallel to the substrate surface. However, in the case of VONPc, a change from standing to lying molecular orientation is observed with increasing film thickness, which increases the absorption intensity in the NIR.

Templated films

In an effort to control the orientation of the NPc films, molecular templating was studied using a thin layer of PTCDA

as a template. Fig. 3a shows the XRD pattern of films of SnNPc deposited on a 20 nm layer of PTCDA at various substrate temperatures. Aside from the peak at 27.5°, which corresponds to PTCDA (Fig. S14, ESI†), the films showed two diffraction peaks at 13.2° and 26.4, which are unequivocally assigned to the 002 and 004 planes, respectively. The intensity of these peaks increases (relative to that of PTCDA) with temperature up to 150 °C, whereupon the peaks diminish. Fig. S15 (ESI†) shows the XRD pattern in different scanning geometries, where the dominant peaks are resolved. The observation of peaks corresponding to lattice planes orthogonal to the 004 plane, namely 020 and 040, further corroborate the structural assignment. The intensity and breadth of the peaks (and thus the crystallinity) were affected not only by the rate and temperature of SnNPc deposition, but also by the rate of the prior PTCDA deposition. Forrest *et al.* have previously shown that the crystallinity of PTCDA is significantly increased at elevated deposition rates up to 15 Å s^{-1}.[32,55] For thin templating films, such fast rates lead to a poor reproducibility of film thickness and, while an increase in the crystallinity of SnNPc was observed for PTCDA rates of 0.1–1 Å s^{-1}, no significant difference was observed between 1 and 2 Å s^{-1}, and so a rate of 1 Å s^{-1} was adopted throughout.

Fig. 3b and c show the AFM images of the templating layer of PTCDA and a templated film of SnNPc deposited at 150 °C, respectively. At 150 °C, the morphology of the templated film is highly crystalline, with block-shaped crystallites of dimensions >150 nm. While crystallinity is observed in the untemplated films only at 200 °C, crystalline features for the templated films are still observed for depositions down to room temperature (Fig. S16, ESI†), which is in distinct contrast to the amorphous texture of the untemplated films at room temperature (*cf.* Fig. S6, ESI†). Fig. 3d shows the absorption spectra of the templated films. The spectra show the same two bands in the NIR as for the untemplated films. However, for the templated films, the relative peak heights are strongly affected by temperature. With increasing deposition temperature, the low energy band increases in intensity up to 150 °C with an associated red-shift to 910 nm. These spectral characteristics are reminiscent of the untemplated films of VONPc, where the increase in Q-band intensity for thicker films was correlated with a molecular plane parallel to the substrate, and thus normal to the incident beam. At 200 °C, the Q-band is diminished, and includes a shoulder band on its low energy tail. Since no other peaks are observed in its XRD profile, it is possible that the underlying PTCDA layer becomes unstable at a high substrate temperature, leading to a decrease in templating efficiency. This conclusion is supported by the decrease in crystallite size observed at 200 °C, compared to 150 °C (Fig. S16, ESI†).

In the case of VONPc, a templating layer of PTCDA was also shown to favor perpendicular stacking, yielding a strong diffraction at 26.4°, as for the untemplated films, but with no peak observable at 6° (Fig. S17, ESI†), suggesting a strong uniaxial orientation, as for SnNPc. Molecular templating with PTCDA is therefore shown to be an efficient way of controlling the crystalline orientation of shuttlecock NPcs, and can induce high crystallinity and uniaxial orientation, even down to room temperature. It should be noted that efficient templating of SnNPc was demonstrated on PTCDA films <1 nm, and could also be achieved on various common substrates of varying surface structure, including Ag, Au, Al, ITO and parylene-C (Fig. S18 and Table S3, ESI†).

Molecular templating of SnNPc was not limited to PTCDA, but could also be achieved on the structurally related 3,4,9,10-perylenetetracarboxylic bisbenzimidazole (PTCBI). However, in this case, an elevated substrate temperature of 150 °C was required to induce templated crystallization (Fig. S19, ESI†).

Computational analysis of the absorption spectra

In an effort to understand the changes observed in the NIR band of the thin film absorption spectra, depending on the substrate treatment, TD-DFT calculations were performed using different cluster models. First, the SnNPc monomer was investigated, optimized in solvent conditions. Fig. 4a shows the

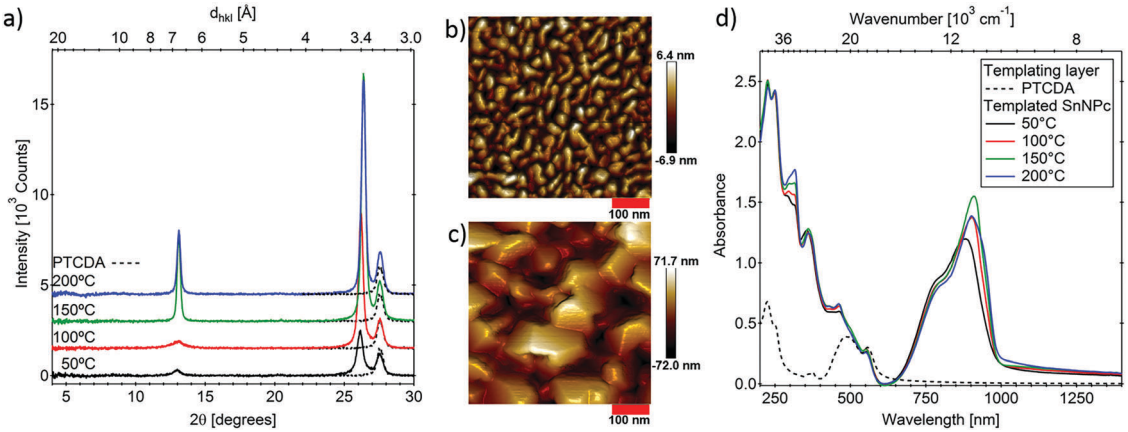

Fig. 3 Characterization of thin films of SnNPc (100 nm, rate 0.1 Å s^{-1}) grown on a 20 nm film of PTCDA (broken line in both graphs) at various substrate temperatures: (a) thin film XRD on SiO_2 substrates (data offset for clarity); (b and c) AFM images of (b) the templating layer of PTCDA, and (c) the templated film of SnNPc grown at a substrate temperature of 150 °C, red scale bars indicate 100 nm; (d) thin film absorption spectra on quartz substrates (solid lines), compared to the thin film spectrum of the templating layer of PTCDA (broken line).

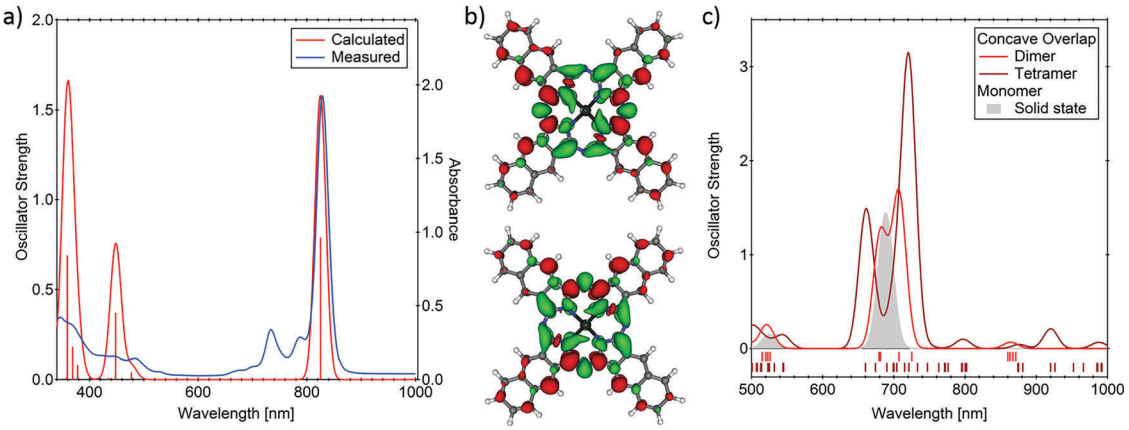

Fig. 4 Computational data of SnNPc showing: (a) comparison between calculated and measured absorption spectra in 1-chloronaphthalene; (b) electron density difference between the ground state and the excited states of the two degenerate transitions at 825 nm (green areas are electronically enriched and red areas are electronically impoverished upon excitation); (c) calculated spectra of concave dimer and tetramer clusters, compared to the solid state optimized monomer, showing increased splitting of the Q-band with increasing nearest neighbor interactions. The ticks indicate the energy of the transitions in the dimer and tetramer models.

calculated spectrum, which exhibits an intense absorption band at 825 nm, close to the experimental value of 829 nm. No other transitions are present up to the second band at 488 nm, which is weakly absorbing. The peak at 825 nm corresponds to two degenerate π–π* transitions (HOMO–LUMO and HOMO–LUMO+1), localized on the naphthalocyanine moiety, with a net increase (decrease) of electron density in the inner (outer) regions (see Fig. 4b). The energy of these transitions depends strongly on (i) the molecular distortion and (ii) the environment. To quantify these effects, two additional spectra were computed on the monomer optimized in the solid-phase, with the spectra computed in solvent or in the gas phase. The main peak is found at 775 and 689 nm, respectively (Fig. S20, ESI†). Compared to the solvent optimized structure, the geometry distortion in the solid phase (spectrum in solution) induces a blue-shift of 50 nm. In turn, the second effect is unveiled by removing the electrostatic effect of the PCM model solvent, which leads to a further blue-shift of up to 90 nm. This demonstrates how sensitive this low-energy peak is to the description of the environment.

Mizuguchi *et al.* have argued that the peak splitting observed in the analogous Phase I TiOPc can be accounted for by the molecular distortion induced in the solid state that removes the degeneracy of the HOMO–LUMO and HOMO–LUMO+1 transitions.[19] However, while peak splitting is observed in the solid-phase optimized monomer spectra, the splitting is small (5 nm (105 cm^{-1}) and 2 nm (33 cm^{-1}) for gas and solvent conditions, respectively) and the two transitions generating the NIR peak remain quasi-degenerate in both these calculations (even if the C_{4v} symmetry is broken). The monomer approach does not adequately explain the splitting of the low-energy band observed in the measured spectra of the untemplated and templated films (*cf.* Fig. 2d and 3d). To investigate this issue further, we computed the absorption spectra of selected SnNPc dimers and tetramers describing the concave and convex inter-layer arrangements (*cf.* Fig. 1d and Fig. S21a, b, ESI†). The TD-DFT spectra of these clusters are shown in Fig. 4c (concave) and Fig. S21c (ESI†) (convex), and are considerably different from that of the SnNPc monomer, showing a large splitting of the low-energy band due to the delocalization of the electronic transition on the two/four molecules. The π–π* nature of the low-energy peak remains, but the shape gains complexity as the number of molecules increases. The frontier orbitals are the bonding and anti-bonding combination of the molecular HOMO and LUMO orbitals. For the dimers, this generates a set of eight transitions ranging from 670 to 880 nm, the lowest energy four being almost dark. For the tetramers, the combination generates 32 transitions ranging from 660 to 992 nm, only two of them being bright (721/746 nm and 660/670 nm, concave/convex). It should be noted that the tetramers show a greater splitting between the two most-intense peaks (*ca.* 60–70 nm, ∼1300 cm^{-1}) than the dimers (*ca.* 20–40 nm, ∼600 cm^{-1}), and a larger red shift of the main band. Overall, the calculations retrieve the qualitative experimental results with a very intense peak followed by a second one less intense. Several weak satellite transitions are present especially at lower energy, which explain the long tails observed above 1000 nm in the measured spectra (*cf.* Fig. 2d and 3d). However, we do not retrieve the exact position of the main bands: the theoretical peaks appear blue shifted (720/745 nm and 661/674 nm for concave/convex tetramers) compared to the experimental peaks (825 and 775 nm). This is due to the limitations of our cluster model in describing the solid state of the material. The results of the computational analysis are tabulated in Table S4 (ESI†), together with the peak positions of the deconvoluted experimental spectra discussed in this work (Table S5 and Fig. S22, ESI†).

Device performance

For device application, control over the degree of crystallinity, as well as the crystalline orientation and packing is essential. The effects of these modifications were assessed in photodetector

devices of the structure metal/insulator/semiconductor/metal (MISM).[38] In such devices, the presence of an insulator layer yields a transient photocurrent response to the change in voltage across the semiconductor layer, induced by illumination, due to capacitive charging/discharging of the insulator dielectric. For devices where the insulator layer is an electrolyte, such as an ionic liquid (IL), the photocurrent transient rise time is in general correlated with the charging of the active layer capacitor, and the decay time with the charging of the insulator layer capacitor.[49,56] As such, the observed photocurrent is highly sensitive to the rate of charge transfer within the active semiconductor layer. It should be noted that, while the low frequency transient waveform does not resemble the square-wave input light signal, as the frequency of the signal is increased beyond the decay time of the transient, the waveform changes to a "pseudo" square-wave response over some range of frequencies (device bandwidth) before decaying once the rise time of the transient is exceeded.[57]

SnNPc is shown to operate as a p-type semiconductor with a modest field effect mobility $\mu + \approx 5 \times 10^{-5}$ cm^2 V^{-1} s^{-1} (see Fig. S23, ESI†). Therefore, by extension to previous studies of IL-MISM devices based on VONPc[39] and other p-type semiconductors,[49] a device architecture of ITO/SnNPc/IL/Ag, where the workfunction of the semiconductor (SC) electrode $\varphi_{SC} > \varphi_{Ag}$, would be expected to yield an accumulation of electrons at the SnNPc/IL interface upon illumination, with the transfer of holes towards the ITO (see Fig. 5a). However, the presence of a thick templating layer of the n-type PTCDA would yield a type II planar p/n heterojunction at the SnNPc/PTCDA interface, blocking the transfer of holes, and favoring rather the transfer of electrons to the PTCDA. Therefore, in order to compare the photoresponse of a standing and lying molecular geometry for SnNPc, the photocurrent waveforms and action spectra were measured for SnNPc deposited on ITO at 150 °C in the presence and absence of an ultra-thin (1 nm) layer of PTCDA, through which the holes would be able to pass through pinholes/defects, or *via* tunneling.[35]

Fig. 5b shows the photocurrent waveform for IL-MISM devices with and without a templating layer of PTCDA (where the IL is MEMP-TFSI). In both cases, a positive transient is observed with light "on", confirming the accumulation of electrons at the SnNPc/IL interface. While the magnitude of photoresponse for the templated device is about half that of the untemplated device, suggesting a lower photovoltage generated across the SC layer (*vide infra*), the rise time of the photocurrent response is significantly increased ($\tau \approx 20$ μs, compared to 1.3 ms for pure SnNPc). As a result, the templated device shows an improved bandwidth from <2 kHz to ~ 50 kHz (defined as the point at which the photocurrent response falls below half that at square-wave),[57] corresponding to a reduced RC component for the SC layer,[49,56] and implying a significant improvement to charge transfer across the templated film.

Despite the reduction in the photocurrent maximum for the templated device, the extracted charge (area under the peaks) in both devices is relatively similar due to the long tail on the photocurrent decay of the templated device. This latter point would indicate a larger RC component to the IL dielectric, which is consistent with the larger surface area of the templated film (*cf.* Fig. 2b and 3c) leading to a larger geometric capacitance. Accordingly, the voltage change must be reduced in the templated device for a similar developed charge. It should be noted that in the case of the pure SnNPc devices, decreasing the deposition temperature from 150 °C to 50 °C resulted in a modest shortening of the photocurrent decay time (consistent with its lower roughness and thus decreased geometric capacitance), but with the photocurrent rise time hardly affected.

Fig. 5c shows the wavelength-dependent photocurrent action spectra for the templated and untemplated devices deposited at 150 °C. A slight broadening to the low-energy side of the NIR photocurrent peak is observed for the templated device. However, both spectra show a similar maximum to their responsivity at ~ 830 nm, and thus the decrease in photoresponse for the templated device in Fig. 5b cannot be accounted for by the spectral shift observed in its absorption spectrum.

The presence of even a thin layer of PTCDA on an electrode surface is known to change the electronic structure at the

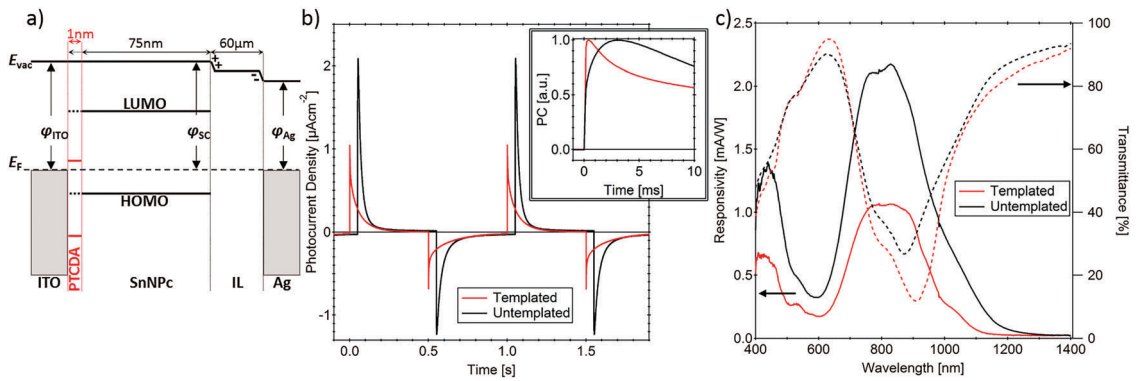

Fig. 5 Photodetector characterization of ITO/SnNPc(75 nm)/IL(MEMP-TFSI)/Ag devices (black), compared to identical devices with an ultra-thin (1 nm) layer of PTCDA to induce templated growth of the SnNPc (red): (a) a qualitative energy level diagram of the component layers in the IL-MISM devices (assuming vacuum level alignment); (b) photocurrent response to periodic square-wave modulated LED illumination (λ = 850 nm, f = 1 Hz, data offset in x-axis for clarity), where the positive signal corresponds to light "on". Inset: Expansion of normalized photocurrent rise; (c) photocurrent action spectra for the devices (solid lines) compared to the transmission spectra of thin films deposited on quartz substrates (broken lines).

electrode/semiconductor interface,[58] which can indirectly affect the device performance through a change in $\Delta\varphi$ across the device. In the responsivity spectrum of the templated device, a non-negligible peak is observed in the region of PTCDA absorption (Fig. 5c), suggesting some direct contribution of the PTCDA to the photocurrent response, even at 1 nm layer thickness. Its positive contribution to the responsivity spectrum suggests the extraction of holes at the ITO/PTCDA interface, with the accumulation of electrons at the PTCDA/SnNPc interface. Such a situation could result in a downwards shift of the vacuum level for SnNPc due to accumulated trapped holes at the SnNPc/PTCDA interface, thus reducing the apparent workfunction of the semiconductor electrode, and thereby decreasing the maximum achievable photovoltage developed in the device.[35,36] The role of PTCDA on the photovoltage can clearly be seen in the photocurrent waveform for thicker PTCDA layers, as shown in Fig. S24 (ESI†). As the PTCDA thickness is increased, the transient peak is further suppressed, and eventually inverts. Careful observation shows the superposition of a positive and negative component to the peak for a 20 nm layer of PTCDA, suggesting that charge separation is occurring at both the SnNPc/IL interface, and the SnNPc/PTCDA interface, with opposite polarity. Efforts are ongoing to avoid the suppression of the photovoltage in the templated devices by pinning the semiconductor Fermi levels to a high workfunction interlayer, such as MoO_x,[36] or by introduction of a blocking contact at the metal/semiconductor interface.

While the above argument can qualitatively explain the observed results, detailed examination of the energy levels would be necessary through combined experiments of X-ray and ultraviolet photoemission spectroscopy to develop a quantitative picture of the device.[59,60] Furthermore, the above description ignores the role of molecular orientation on the energy levels of an organic film, which have also been shown to affect the device energetics.[61,62] Some indication of the importance of crystallinity and crystalline orientation can be seen in devices fabricated with the solvent annealed films (see Fig. S25, ESI†). While their photocurrent action spectra follow well the trends in their absorption profiles, the photocurrent waveform is strongly affected by the solvent used for pre-treatment, both in terms of response speed, but also response polarity. These data clearly show that the degree of crystallinity and crystalline orientation can change the relative energetics in the device, either through a change in energy level alignment between the semiconductor and the electrode, or progressively throughout the film. However, further studies are necessary to correlate these data with the crystalline structures developed in the films under SVA.

Conclusions

SnNPc absorbs strongly in the NIR region making it of technological relevance for photovoltaic application, as well as for optical data transmission and storage. In this work, the thin film properties of SnNPc were investigated and strategies for controlling the crystallinity and crystalline orientation within the films were developed. The thin film absorption properties are shown to be strongly dependent on the growth conditions, as well as substrate pre- and post-treatment. Molecular templating from a thin layer of PTCDA (or PTCBI) induce a lying molecular geometry with a crystalline phase analogous to Phase I of TiOPc. This effect is independent of the substrate material, and results in an enhanced absorption in the NIR and drastically improves the bandwidth of transient MISM photodetector devices. Furthermore, through the use of solvent vapor annealing, different polymorphs are accessible, which show a significant red (or blue) shift to the Q-band absorption, and can be used to extend light harvesting deeper into the NIR. Work is ongoing to identify the distinct crystalline phases induced by solvent vapor annealing, as well as to develop the performance of SnNPc based optoelectronic devices.

Author contribution

The manuscript was written through contributions of all authors. All authors have given approval to the final version of the manuscript.

Conflicts of interest

The authors declare no competing financial interest.

Acknowledgements

We are grateful to the Ministry of Education, Culture, Sports and Technology (MEXT) of Japan for a Grant-in-Aid for Young Scientists to SD (16K17971) and LR (16K17853). LR would like to thank the JST-ERATO Itami Molecular Nanocarbon Project for use of AFM facilities. YS and KA acknowledge the financial support of a Grant-in-Aid for Scientific Research from MEXT, and of the JSPS Core-to-Core Program, A. Advanced Research Networks. SV acknowledges the LabEx-Chemistry of Complex Systems for the post-doctoral grant ANR-10LABX-0026CSC. CG and SV acknowledge the regional High-Performance Computing (HPC) center in Strasbourg for computational resources.

References

1 J.-L. Brédas, J. P. Calbert, D. A. da Silva and J. Cornil, Organic semiconductors: A Theoretical Characterization of the Basic Parameters Governing Charge Transport, *Proc. Natl. Acad. Sci. U. S. A.*, 2002, **99**, 5804–5809.
2 H. Moon, R. Zeis, E.-J. Borkent, C. Besnard, A. J. Lovinger, T. Siegrist, C. Kloc and Z. Bao, Synthesis, Crystal Structure, and Transistor Performance of Tetracene Derivatives, *J. Am. Chem. Soc.*, 2004, **126**, 15322–15323.
3 J. E. Anthony, Functionalized Acenes and Heteroacenes for Organic Electronics, *Chem. Rev.*, 2006, **106**, 5028–5048.

4 C. Reese and Z. Bao, Organic Single Crystals: Tools for the Exploration of Charge Transport Phenomena in Organic Materials, *J. Mater. Chem.*, 2006, **16**, 329–333.
5 J. Cornil, D. Beljonne, J. P. Calbert and J.-L. Brédas, Interchain Interactions in Organic π-Conjugated Materials: Impact on Electronic Structure, Optical Response, and Charge Transport, *Adv. Mater.*, 2001, **13**, 1053–1067.
6 V. C. Sundar, J. Zaumseil, V. Podzorov, E. Menard, R. L. Willett, T. Someya, M. E. Gershenson and J. A. Rogers, Elastomeric Transistor Stamps: Reversible Probing of Charge Transport in Organic Crystals, *Science*, 2004, **303**, 1644–1646.
7 J. Y. Lee, S. Roth and Y. W. Park, Anisotropic Field Effect Mobility in Single Crystal Pentacene, *Appl. Phys. Lett.*, 2006, **88**, 252106.
8 B. P. Rand, D. Cheyns, K. Vasseur, N. C. Giebink, S. Mothy, Y. Yi, V. Coropceanu, D. Beljonne, J. Cornil, J.-L. Brédas and J. Genoe, The Impact of Molecular Orientation on the Photovoltaic Properties of a Phthalocyanine/Fullerene Heterojunction, *Adv. Funct. Mater.*, 2012, **22**, 2987–2995.
9 H.-C. Lin, G. A. MacDonald, Y. Shi, N. W. Polaske, D. V. McGrath, S. R. Marder, N. R. Armstrong, E. L. Ratcliff and S. S. Saavedra, Influence of Molecular Orientation on Charge-Transfer Processes at Phthalocyanine/Metal Oxide Interfaces and Relationship to Organic Photovoltaic Performance, *J. Phys. Chem. C*, 2015, **119**, 10304–10313.
10 R. D. Gould, Structure and Electrical Conduction Properties of Phthalocyanine Thin Films, *Coord. Chem. Rev.*, 1996, **156**, 237–274.
11 *Phthalocyanines: Properties and Applications*, ed. C. C. Leznoff and A. B. P. Lever, VCH, New York, 1996, vol. 4.
12 S. M. Bayliss, S. Heutz, G. Rumbles and T. S. Jones, Thin Film Properties and Surface Morphology of Metal Free Phthalocyanine Films Grown by Organic Molecular Beam Deposition, *Phys. Chem. Chem. Phys.*, 1999, **1**, 3673–3676.
13 W. Hiller, J. Strähle, W. Kobel and M. Hanack, Polymorphie, Leitfähigkeit und Kristallstrukturen von Oxo-phthalocyaninato-titan(IV), *Z. Kristallogr.*, 1982, **159**, 173–183.
14 K. Oka, O. Okada and K. Nukada, Study of the Crystal Structure of Titanylphthalocyanine by Rietveld Analysis and Intermolecular Energy Minimization Method, *Jpn. J. Appl. Phys.*, 1992, **31**, 2181–2184.
15 H. Yonehara, K. Ogawa, H. Etori and C. Pac, Vapor Deposition of Oxotitanium(IV) Phthalocyanine on Surface-Modified Substrates: Effects of Organic Surfaces on Molecular Alignment, *Langmuir*, 2002, **18**, 7557–7563.
16 N. Coppedè, M. Castriota, E. Cazzanelli, S. Forti, G. Tarabella, T. Toccoli, K. Walzer and S. Iannotta, Controlled Polymorphism in Titanyl Phthalocyanine on Mica by Hyperthermal Beams: A Micro-Raman Analysis, *J. Phys. Chem. C*, 2010, **114**, 7038–77044.
17 T. Saito, W. Sisk, T. Kobayashi, S. Suzuki and T. Iwayanagi, Photocarrier Generation Processes of Phthalocyanines Studied by Photocurrent and Electroabsorption Measurements, *J. Phys. Chem.*, 1993, **97**, 8026–8031.
18 T. Saito, Y. Iwakabe, T. Kobayashi, S. Suzuki and T. Iwayanagi, Thermochromism of Specific Crystal Form Oxotitanium Phthalocyanines Studied by Electroabsorption and X-ray Diffraction Measurements, *J. Phys. Chem.*, 1994, **98**, 2726–2728.
19 J. Mizuguchi, G. Rihs and H. R. Karfunkel, Solid-State Spectra of Titanylphthalocyanine as Viewed from Molecular Distortion, *J. Phys. Chem.*, 1995, **99**, 16217–16227.
20 D. Placencia, W. Wang, R. C. Shallcross, K. W. Nebesny, M. Brumbach and N. R. Armstrong, Organic Photovoltaic Cells Based On Solvent-Annealed, Textured Titanyl Phthalocyanine/C_{60} Heterojunctions, *Adv. Funct. Mater.*, 2009, **19**, 1913–1921.
21 D. Placencia, W. Wang, J. Gantz, J. L. Jenkins and N. R. Armstrong, Highly Photoactive Titanyl Phthalocyanine Polymorphs as Textured Donor Layers in Organic Solar Cells, *J. Phys. Chem. C*, 2011, **115**, 18873–18884.
22 K. Vasseur, B. P. Rand, D. Cheyns, L. Froyen and P. Heremans, Structural Evolution of Evaporated Lead Phthalocyanine Thin Films for Near-Infrared Sensitive Solar Cells, *Chem. Mater.*, 2011, **23**, 886–895.
23 K. Vasseur, B. P. Rand, D. Cheyns, K. Temst, L. Froyen and P. Heremans, Correlating the Polymorphism of Titanyl Phthalocyanine Thin Films with Solar Cell Performance, *J. Phys. Chem. Lett.*, 2012, **3**, 2395–2400.
24 M. L. Kaplan, A. J. Lovinger, W. D. Reents, Jr. and P. H. Schmidt, The Preparation, Spectral Properties, and X-ray Structural Features of 2,3-Naphthalocyanines, *Mol. Cryst. Liq. Cryst.*, 1984, **112**, 345–358.
25 K. Morishige and K. Araki, Crystal Structures of Nickel, Copper and Zinc Naphthalocyaninates, *J. Chem. Soc., Dalton Trans.*, 1996, 4303–4305.
26 H. Yanagi, T. Kouzeki, M. Ashida, T. Noguchi, A. Manivannan, K. Hashimoto and A. Fujishima, Molecular Orientation of Vacuum-Deposited Thin Films of Zinc-naphthalocyanine, *J. Appl. Phys.*, 1992, **71**, 5146–5153.
27 H. Yanagi, M. Ashida, J. Elbe and D. Wöhrle, Crystal Growth and Molecular Orientation of Vanadylnaphthalocyanine in Thin Films, *J. Phys. Chem.*, 1990, **94**, 7056–7061.
28 J. Yang and D. Yan, Weak Epitaxy Growth of Organic Semiconductor Thin Films, *Chem. Soc. Rev.*, 2009, **38**, 2634–2645.
29 J. Yang, D. Yan and T. S. Jones, Molecular Template Growth and its Applications in Organic Electronics and Optoelectronics, *Chem. Rev.*, 2015, **115**, 5570–5603.
30 S. R. Forrest, P. E. Burrows, E. I. Haskal and F. F. So, Ultrahigh-Vacuum Quasiepitaxial Growth of Model van der Waals Thin Films. II. Experiment, *Phys. Rev. B: Condens. Matter Mater. Phys.*, 1994, **49**, 11309.
31 K. Eguchi, C. Nanjo, K. Awaga, H.-H. Tseng, P. Robaschik and S. Heutz, Highly-Oriented Molecular Arrangements and Enhanced Magnetic Interactions in Thin Films of CoTTDPz Using PTCDA Templates, *Phys. Chem. Chem. Phys.*, 2016, **18**, 17360–17365.
32 A. J. Lovinger, S. R. Forrest, M. L. Kaplan, P. H. Schmidt and T. Venkatesan, Structural and Morphological Investigation

of the Development of Electrical Conductivity in Ion-Irradiated Thin Films of an Organic Material, *J. Appl. Phys.*, 1984, **55**, 476–482.

33 S. Heutz, R. Cloots and T. S. Jones, Structural Templating Effects in Molecular Heterostructures Grown by Organic Molecular-Beam Deposition, *Appl. Phys. Lett.*, 2000, **77**, 3938–3940.

34 S. Heutz and T. S. Jones, Structural and Morphological Modifications in Double Layer Heterostructures Containing H_2Pc, Perylene-3,4,9,10-tetracarboxylic Dianhydride and Alq3, *J. Appl. Phys.*, 2002, **92**, 3039–3046.

35 P. Sullivan, T. S. Jones, A. J. Ferguson and S. Heutz, Structural Templating as a Route to Improved Photovoltaic Performance in Copper Phthalocyanine/Fullerene (C_{60}) Heterojunctions, *Appl. Phys. Lett.*, 2007, **91**, 233114.

36 K. V. Chauhan, P. Sullivan, J. L. Yang and T. S. Jones, Efficient Organic Photovoltaic Cells through Structural Modification of Chloroaluminum Phthalocyanine/Fullerene Heterojunctions, *J. Phys. Chem. C*, 2010, **114**, 3304–3308.

37 B. E. Lassiter, R. R. Lunt, C. K. Renshaw and S. R. Forrest, Structural Templating of Multiple Polycrystalline Layers in Organic Photovoltaic Cells, *Opt. Express*, 2010, **18**, A444–A450.

38 L. Hu, Y. Noda, H. Ito, H. Kishida, A. Nakamura and K. Awaga, Optoelectronic Conversion by Polarization Current, Triggered by Space Charges at Organic-Based Interfaces, *Appl. Phys. Lett.*, 2010, **96**, 243303.

39 S. Dalgleish, L. Reissig, L. Hu, M. M. Matsushita, Y. Sudo and K. Awaga, Factors Affecting the Stability and Performance of Ionic Liquid-Based Planar Transient Photodetectors, *Langmuir*, 2015, **31**, 5235–5243.

40 CrystalClear & CrystalStructure, Rigaku Corporation, Tokyo, Japan.

41 SHELXL Version 2016/4: Sheldrick, G. M. A Short History of SHELX, *Acta Cryst.*, 2008, **A64**, 112–122.

42 Global Fit Version 2.0 & PDXL Version 1.8.1, Rigaku Corporation, Tokyo, Japan.

43 NanoScope Analysis Version 1.5, Bruker Corporation, Santa Barbara, U.S.

44 P. J. Stephens, F. J. Devlin, C. F. Chabalowski and M. J. Frisch, Ab Initio Calculation of Vibrational Absorption and Circular Dichroism Spectra Using Density Functional Force Fields, *J. Phys. Chem.*, 1994, **98**, 11623–11627.

45 E. van Lenthe, A. E. Ehlers and E. J. Baerends, Geometry Optimizations in the Zero Order Regular Approximation for Relativistic Effects, *J. Chem. Phys.*, 1999, **110**, 8943–8953.

46 E. van Lenthe and E. J. Baerends, Optimized Slater-Type Basis Sets for the Elements 1–118, *J. Comput. Chem.*, 2003, **24**, 1142–1156.

47 G. te Velde, F. M. Bickelhaupt, E. J. Baerends, C. Fonseca Guerra, S. J. A. van Gisbergen, J. G. Snijders and T. Ziegler, Chemistry with ADF, *J. Comput. Chem.*, 2001, **22**, 931–967.

48 M. Kohout, *DGrid, version 4.6*, Radebeul, 2011.

49 L. Reissig, K. Mori, R. Treadwell, S. Dalgleish and K. Awaga, Factors Affecting the Polarity and Magnitude of Photoresponse of Transient Photodetectors, *Phys. Chem. Chem. Phys.*, 2016, **18**, 6821–6830.

50 M. K. Friedel, B. F. Hoskins, R. L. Martin and S. A. Mason, A New Metal(II) Phthalocyanine Structure: X-ray and Mössbauer Studies of the Triclinic Tin(II) Phthalocyanine, *J. Chem. Soc. D*, 1970, 400–401.

51 R. Kubiak and J. Janczak, X-ray Analysis of Phthalocyanines Formed in the Reaction of Au-Cu and Au-Sn Alloys with 1,2-Dicyanobenzene, *J. Alloys Compd.*, 1992, **189**, 107–111.

52 T. Inabe, Design of Functional Molecular Crystals by Controlling Intermolecular Interactions, *Bull. Chem. Soc. Jpn.*, 2005, **78**, 1373–1383.

53 R. F. Ziolo, C. H. Griffiths and J. M. Troup, Crystal Structure of Vanadyl Phthalocyanine, Phase II, *J. Chem. Soc., Dalton Trans.*, 1980, 2300–2302.

54 E. Jakubikova, I. H. Campbell and R. L. Martin, Effects of Peripheral and Axial Substitutions on Electronic Transitions of Tin Naphthalocyanines, *J. Phys. Chem. A*, 2011, **115**, 9265–9272.

55 S. R. Forrest, M. L. Kaplan and P. H. Schmidt, Organic-on-Inorganic Semiconductor Contact Barrier Diodes. II. Dependence on Organic Film and Metal Contact Properties, *J. Appl. Phys.*, 1984, **56**, 543–551.

56 L. Reissig, S. Dalgleish and K. Awaga, A differential Photodetector: Detecting Light Modulations Using Transient Photocurrents, *AIP Adv.*, 2016, **6**, 015306.

57 S. Dalgleish, M. M. Matsushita, L. Hu, B. Li, H. Yoshikawa and K. Awaga, Utilizing Photocurrent Transients for Dithiolene-Based Photodetection: Stepwise Improvements at Communications Relevant Wavelengths, *J. Am. Chem. Soc.*, 2012, **134**, 12742–12750.

58 R. Schlaf, P. G. Schroeder, M. W. Nelson, B. A. Parkinson, P. A. Lee, K. W. Nebesny and N. R. Armstrong, Observation of Strong Band Bending in Perylene Tetracarboxylic Dianhydride Thin Films Grown on SnS_2, *J. Appl. Phys.*, 1999, **86**, 1499–1509.

59 M. Oehzelt, K. Akaike, N. Koch and G. Heimel, Energy-Level Alignment at Organic Heterointerfaces, *Sci. Adv.*, 2015, **1**, e1501127.

60 A. Opitz, A. Wilke, P. Amsalem, M. Oehzelt, R.-P. Blum, J. P. Rabe, T. Mizokuro, U. Hörmann, R. Hansson, E. Moons and N. Koch, Organic Heterojunctions: Contact-Induced Molecular Reorientation, Interface States, and Charge Re-Distribution, *Sci. Rep.*, 2016, **6**, 21291.

61 W. Chen, D. C. Qi, H. Huang, Y. Z. Wang, S. Chen, X. Y. Gao and A. T. S. Wee, Molecular Orientation Dependent Energy Level Alignment at Organic–Organic Heterojunction Interfaces, *J. Phys. Chem. C*, 2009, **113**, 12832–12839.

62 G. Heimel, I. Salzmann, S. Duhm and N. Koch, Design of Organic Semiconductors from Molecular Electrostatics, *Chem. Mater.*, 2011, **23**, 359–377.

